1989

Optical Recording Aspects of rf Magnetron Sputtered Iron-Garnet Films

J.P. Krumme

V. Doormann

P. Hansen

H. Baumgart
Old Dominion University, hbaumgar@odu.edu

J. Petruzzello

See next page for additional authors

Original Publication Citation

Krumme, J.-P., Doormann, V., Hansen, P., Baumgart, H., Petruzzello, J., & Viegers, M. P. A. (1989). Optical recording aspects of rf magnetron-sputtered iron-garnet films. *Journal of Applied Physics*, 66(9), 4393-4407. doi:10.1063/1.343934

Optical recording aspects of rf magnetron-sputtered iron-garnet films

J.-P. Krumme, V. Doormann, and P. Hansen
Philips GmbH, Forschungslaboratorium Hamburg, D-2000 Hamburg 54, Federal Republic of Germany

H. Baumgart and J. Petruzzello
North American Philips Corporation, Research Lab, Briarcliff Manor, New York 10510

M. P. A. Viegers
Philips Research Labs, NL-5600 JA Eindhoven, The Netherlands

(Received 19 April 1989; accepted for publication 24 July 1989)

The intrinsic magneto-optical readout performance in reflection is calculated for bismuth and cobalt-substituted iron-garnet films on a multilayer interference mirror at 800-, 633-, 488-, and 420-nm wavelengths and is compared with that of a trilayer medium composed of an antireflection layer, a rare-earth transition-metal film, and a metallic mirror. It is found, when disregarding inhomogeneities, like irregular domain shape, ripple of the magnetic anisotropy, and surface roughness, that iron garnets are superior to rare-earth transition-metal films at blue to near-ultraviolet wavelengths if operated at thicknesses where optical interference occurs in the magnetic layer. Optical transmittance at these thicknesses is sufficiently high so that multilevel recording media can be conceived. In contrast, the optical absorption of rare-earth transition-metal alloys is much higher so that only thicknesses much above interference conditions are feasible, thus precluding them from multilevel recording. This comparative study is supplemented by calculating the magneto-optical performance in reflection of a recently reported multilayer medium composed of an antireflection coating and a periodically repeated sandwich of 4-Å Co and 9-Å Pt layers. In contrast to conventional rare-earth transition-metal films, the magneto-optical Kerr effects of this material do not degrade when decreasing the wavelength from 800 to 400 nm, but still do not reach the performance of bismuth-iron garnets in the green to ultraviolet spectrum. For the garnet system $Y_{3-x}Bi_xFe_5O_{12}$ the spectra of the real and imaginary parts of the diagonal and off-diagonal component of the dielectric tensor ϵ_{ij} are reported in the range of photon energies between 1 and 5 eV, i.e., 1240- and 248-nm wavelengths and a bismuth concentration up $x = 1.4$ Bi^{3+} atoms per garnet formula. In addition, the off-diagonal components ϵ'_{12} and ϵ''_{12} are parametrized in terms of paramagnetic optical transitions, taking the spectra for $x = 1.25$ as a typical example. Furthermore, optical and magneto-optical spectra are presented for Co^{2+}- and Co^{3+}- substituted iron garnets and barium hexaferrite $BaFe_{12}O_{19}$. Finally, the spectral dependence of the magneto-optical figure of merit $2\Theta_F/\alpha$ of $(Y,Bi)_3Fe_5O_{12}$ and amorphous TbFe is compared. Furthermore, high-resolution transmission electron micrographs and x-ray double-crystal diffractograms are presented that elucidate the perfect epitaxial alignment of single-crystalline iron-garnet films and the columnar morphology of polycrystalline iron-garnet films prepared by rf magnetron sputtering. The initial nucleation period of polycrystalline garnet films can be influenced by low-energy ion bombardment for improving the film texture. Under favorable sputtering conditions single- and polycrystalline bismuth-iron garnet films develop a perpendicular magnetic anisotopy. It is not yet clear whether sputtered iron-garnet films can meet the critical requirements on magnetic wall coercivity and magnetic remanence.

I. INTRODUCTION

With the advent of reversible optical recording in non-crystalline rare-earth transition-metal (RETM) films the search for improved storage media is going on concerning stability, storage density, and write-in sensitivity. Within the group of magneto-optical memory materials the crystalline iron oxides, i.e., the cubic garnets, the cubic cobalt ferrites, and the hexagonal barium ferrites are considered as contenders. The iron oxides feature structural stability and favorable optical properties in the visible and near-ultraviolet spectrum. They can be readily prepared by rf sputtering from targets that are relatively easy to fabricate.

Among these three compounds, the polycrystalline hexaferrites exhibit particularly high intrinsic uniaxial magnetic anisotropy and favorable growth morphology, both contributing to the desired magnetic remanence. The fairly high magnetic Curie temperature can be reduced to the level of the iron garnets by diamagnetic substituents, such as Ga^{3+}, Al^{3+}, In^{3+}, and Sc^{3+}. Recording experiments at an 800-nm wavelength resulted in a carrier-to-noise ratio (CNR) at a 30-kHz bandwidth of 50 dB.[1] Processing information on rf sputtering of barium hexaferrites is reported in Refs. 2 and 3.

The iron garnets can be tailored over a fairly wide range of their intrinsic magnetic and optical properties by chemi-

 0021-8979/89/214393-15$02.40

cal substitution. By doing so one can achieve particularly high magneto-optical performance at shorter wavelengths through enhanced spectral transitions of the iron ions; one can realize high write-in sensitivity through lowering their Curie temperature; and one can minimize demagnetizing effects on the magnetic remanence through adjustment of their magnetic compensation temperature. Favorable constituents in the iron garnets for optical recording are bismuth Bi^{3+} ions to enhance their magneto-optical activity and cobalt Co^{2+} ions to increase their optical absorption in the visible spectrum, and dysprosium Dy^{3+} ions to improve the magnetic wall coercivity in polycrystalline films via magnetostriction.[4–6] In spite of their intrinsic cubic symmetry, bismuth-iron garnet films can be prepared with perpendicular magnetic anisotropy, as will be mentioned below. A CNR value of 49 dB has been achieved by Itoh *et al.* in recording experiments with Ar^+ ion laser light at a 514-nm wavelength in 300-nm-thick pyrolytically deposited, randomly crystallized films on glass substrates carrying 1.5-μm-diam bubble domains.[6] Shono *et al.* have reached a CNR value of 57 dB in rf magnetron-sputtered highly (111) textured films on GGG substrates under similar recording conditions.[6]

In the cobalt spinel ferrites prepared by spray pyrolysis a CNR below 35 dB has been achieved and so far interpreted as being due to nonuniform magnetic anisotropy.[7] The compositional variability of this class of materials is limited, similar to the hexaferrites.

In this study, optical and microstructural properties of rf magnetron-sputtered iron-garnet films are discussed with relevance to optical recording. Emphasis is put on the work performed at Philips Research. The magneto-optical performance of iron garnets is compared with that of the hexaferrites, RETM alloys, and Co/Pt multilayers in the near-infrared to near-ultraviolet spectrum. Based on the optical and magneto-optical data reported here the magneto-optical figure of merit of a multilayer film structure is calculated which consists of the garnet layer and a dielectric mirror with 100% reflectivity. If only their intrinsic properties are considered, the iron garnets are found to exhibit significantly better magneto-optical readout performance in reflection at blue to near-ultraviolet wavelengths than RETM films and Co/Pt multilayers. However, other key recording parameters, like wall coercivity H_c and uniaxial magnetic anisotropy K_u, which have been studied by other authors,[5,6] are still critical. For improving the CNR much beyond the reported values, much work has still to be devoted to the mastering of the rf sputtering process in order to meet the system requirements on morphology and magnetic anisotropy of polycrystalline iron-garnet films.

II. SAMPLE PREPARATION

Apart from the polycrystalline Co-substituted $Gd_3Fe_5O_{12}$ (GIG) garnet films, all the single-crystalline samples reported here have already been discussed elsewhere concerning preparation and various physical properties. In particular, the bismuth-substituted GIG films grown by rf magnetron sputter epitaxy are the *same* as presented in Ref. 8; the bismuth-substituted $Y_3Fe_5O_{12}$(YIG) garnet films made by liquid-phase epitaxy (LPE) are the *same* as studied in Refs. 9–11; the barium hexaferrite $BaFe_{12}O_{19}$ film prepared by LPE is the *same* as investigated in Ref. 12; and the barium hexaferrite single-crystal wafers made by solvent growth are the *same* as explored in Ref. 13. Therefore, the reader is referred to those articles from our laboratory for details on the applied technology and the crystal quality.

The polycrystalline Co^{3+}-substituted GIG films have been grown by classical rf diode sputtering from powder targets under similar conditions as reported in Ref. 14. The applied process parameters are listed in Table I. The single-crystalline Co^{2+}-substituted iron-garnet film has been prepared by LPE, the growth conditions are summarized in Table II. The composition of those samples identified here is compiled in Table III.

III. GROWTH OF *IN SITU* CRYSTALLIZING IRON-GARNET FILMS UNDER THE CONDITIONS OF rf MAGNETRON SPUTTERING

Among the preparation techniques used to obtain proper samples needed in the present study, we now consider rf magnetron sputtering in more detail because it is particularly suited for optical recording media.

In situ crystallization in about 1-Pa argon plasma is assumed to proceed as outlined in Fig. 1.[16] At substrate temperatures above about 750 K and growth rates of a few 10^{-1} (nm s^{-1}) bismuth-iron garnet films order epitaxially on sin-

TABLE I. Sputtering parameters of the Co^{3+}-substituted iron-garnet films Nos. 2, 3, and 4.

Sputtering parameters[a]	Film No. 2	Film No. 3	Film No. 4
Target composition	$Gd_3Fe_{4.5}Co_{0.5}O_{12}$	$Gd_3Fe_{4.5}Co_{0.5}O_{12}$	$Gd_{2.78}Fe_{4.25}Co_{0.97}O_{12}$
Sputter gas	O_2, 2 Pa	O_2, 2.2 Pa	O_2, 2.2 Pa
Target potential (V_{rms})	600	600	600
Substrate potential (V_{rms})	85	60	floating
Substrate temperature (K)	725	725	725
rf power (W)	420	400	300
Deposition rate (μm/h)	0.16	0.15	0.11
Film thickness (μm)	2.60	3.40	3.40
Substrate	GGCMZ(111),a_o = 1.2501 nm	GGCMZ(111),a_0 = 1.2501 nm	GGCMZ(111),a_0 = 1.2501 nm
Annealing	O_2, 1 bar, 1073 K, 2 h	O_2, 1 bar 1073 K, 2 h	O_2, 1 bar 1073 K, 2 h

[a] rf diode sputtering conditions otherwise as in Ref. 14.

TABLE II. Growth parameters of the liquid-phase epitaxial Co^{2+}-substituted iron-garnet film No. 5.

Growth parameters[a]	Film No. 5
Growth temp. (K)	1060
Undercooling (K)	$\Delta T_s = 45 (= T_{\text{saturation}} - T_{\text{growth}})$
Film thickness (μm)	10.4
Growth rate (μm/min)	0.52
Misfit ($a_s - a_f^{\perp}$)	~ 0
Melt	[Co]/[Fe] = 0.10, [Ge]/[Fe] = 0.45, T_s = 1105 K
Substrate	Nd-,Mg-,Zr-substituted GGG, a_o = 1.2508 nm

[a] Liquid-phase epitaxial (LPE) growth otherwise as in Ref. 15.

gle-crystalline gallium-garnet substrates beneath an about 1-nm-thick bismuth-enriched segregation zone.[17] Ion migration in this shallow surface region is significantly enhanced by low-energy argon Ar^+ ions accelerated towards the film surface across the adjacent plasma sheath. Their penetration depth is of the order of only 1 atomic monolayer.

The sputtered target species arrive at the film surface as partially ionized and partially thermalized particles and essentially consist of monatomic metal *M*, monatomic oxygen O, and diatomic MO. Saturation of the film lattice with oxygen is maintained due to the oxygen supply from the target and, to a lesser extent, from the residual gas. The argon incorporation in crystalline garnet films is generally below 0.01 atoms per garnet formula [a/gf]. The loss by thermal desorption of monatomic Bi and diatomic O_2, being the least tightly bound constituents in the garnet surface, is negligible provided the rf potential distribution in the sputtering system is strongly asymmetric, the target magnetization is < 30 mT, the substrate is electrically floating, the oxygen level in the noble gas plasma is not more than a few parts per thousand and the noble gas pressure is in the 1-Pa range. Under these favorable growth conditions, rf magnetron sputtered single- and polycrystalline bismuth-iron garnet films develop a uniaxial magnetic anisotropy normal to the growth direction as has been recently discovered.[16]

IV. MICROSTRUCTURE OF *IN SITU* CRYSTALLIZED BISMUTH-IRON GARNET FILMS PREPARED BY rf MAGNETRON SPUTTERING

A. Epitaxial films

Sputter epitaxially grown iron-garnet films of high crystalline quality exhibit the characteristic magnetic domain patterns shown in Figs. 2(a) and 2(b) depending on the sign

TABLE III. Chemical composition in atoms per garnet formula [a/gf] of all specified iron-garnet films, measured by electron-probe microanalysis (EPMA).

Sample No.	Sample composition [a/gf] Y	Gd	Bi	Pb	Fe	Al	Ga	Pt	Co	Ge	Ba	Mn	Ar	Process	Ref.
1	1.69		1.25	0.06	4.97			0.03						LPE	9,10
1a		2.0	1.0		4.4	0.4	0.2							LPE	15
1b		1.97	1.04		4.51	0.26	0.22					0.005		rf magnetron, glass IRG3	
2		3.51			4.17				0.32					rf diode	
3		3.16			4.39				0.45					sputtering	14
4		3.20			3.98				0.93					(Table I)	
5[a]		1.98	0.92	0.10	4.13	0.23	0.19	0.01	0.16	0.27				LPE (Table II)	
6		1.99	1.35		4.12	0.33	0.22						0.01	substrate ion bombarded	
7[b]		2.04	1.24		4.10	0.38	0.24						0.01	rf magnetron sputtering	
8		2.08	0.98		4.12		0.82						0.00	substrate coated with 5 nm amorph. layer; initial substrate bias	8
9		2.10	1.01		4.06		0.83						0.00		
10					11.95						1.04			flux growth	13
11					11.81						1.02	0.17		on hexagaliate seed	
12			0.08		12.00				0.06		0.97			LPE	12

[a] Substrates Nd-, Mg-, Zr-substituted $Gd_3Ga_5O_{12}$(NGGMZ), a_o = 1.2508 nm, (111).
[b] Substrates Ca-, Mg-, Zr-substituted $Gd_3Ga_5O_{12}$(GGCMZ), a_o = 1.2488 nm, (110); all other substrates on (111)Ca-, Mg-, Zr-GGG(GGCMZ), a_o = 1.2501 nm.

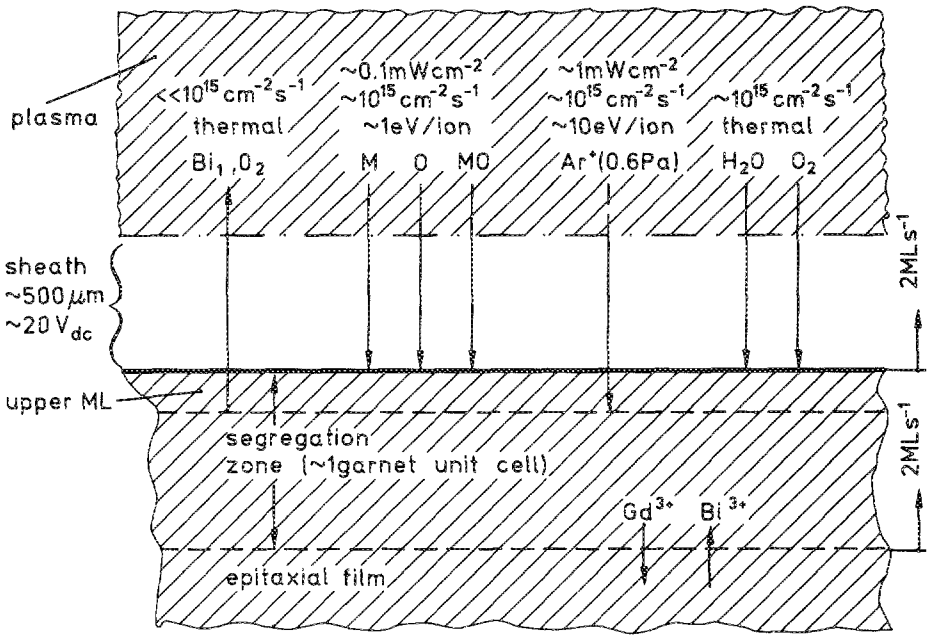

FIG. 1. Schematic representation of epitaxial growth of bismuth-substituted iron-garnet films by rf magnetron sputtering under favorable conditions. The major species interacting with the growing film surface are indicated; ML denotes monolayer; *M*, monatomic metal; and MO, diatomic metal oxide species sputtered from the target (see Refs. 16 and 17).

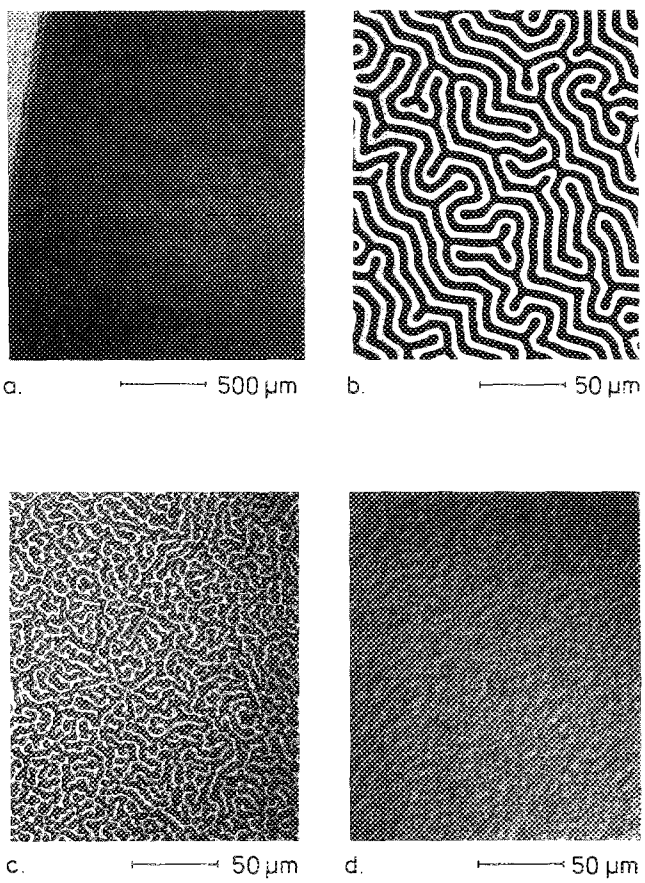

FIG. 2. Transmission photomicrographs of typical magnetic domain patterns (a,b,c) of rf magnetron sputtered epitaxial (a,b) and *in situ* polycrystalline (c) bismuth-substituted iron-garnet films using polarized light and a reflection photomicrograph (d) of film (c). Films (a) and (b) are grown under compressive lattice misfit stress. Film (a) is grown at 770 K without and films (b) and (c) are grown at 830 K with perpendicular growth-induced magnetic anisotropy. Film (c,d) is grown on an ion-bombarded gallium-garnet substrate.

of the uniaxial magnetic anisotropy constant K_u. Their magnetic wall coercivity H_c is as low as that of magnetic bubble memory materials, as deduced from the magnetic hysteresis curve (1) in Fig. 3. Optical waveguide losses in the 1.3–1.5-nm wavelength range and the x-ray diffraction linewidth are extremely small,[8] confirming oxygen saturation and crystal perfection. Within the lattice misfit range $-1.9 \leqslant \Delta a^{\perp}/a_o \times 10^{-2} \leqslant 0.4$ the strain-induced magnetic and optical anisotropies behave strictly linearly with $\Delta a^{\perp}$ (Ref. 8), confirming the epitaxial alignment of the film with the substrate lattice. The quantity $\Delta a^{\perp} = a_s - a_f^{\perp}$ is defined as the difference between the free lattice constant a_s of the substrate and the perpendicular lattice constant $a_f^{\perp}$ of the strained film.

The smooth pattern of cleaved cross sections normal to the epitaxial film plane resembles that of glassy amorphous films, as can be seen in the scanning electron microscope (SEM) picture of Fig. 4(a). Transmission electron micrographs (TEM) of cross sections through the film/substrate

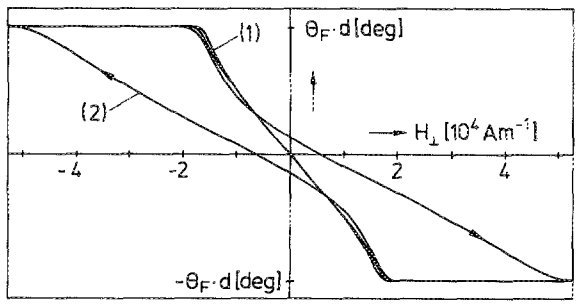

FIG. 3. Magnetic hysteresis curves of an epitaxial (1) and a polycrystalline (2) rf magnetron-sputtered bismuth-iron garnet film with perpendicular magnetic anisotropy measured by the magneto-optical Faraday rotation Θ_F using a light spot much larger than the domain size. *d* denotes the film thickness.

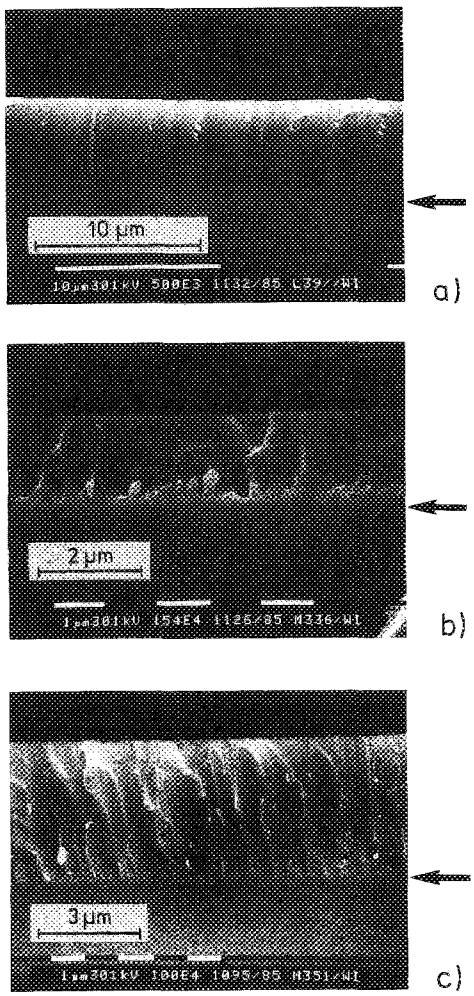

FIG. 4. Scanning electron micrographs (SEM) of cleaved cross sections through bismuth-iron garnet films grown by liquid-phase epitaxy (LPE) (a) and by rf magnetron sputtering (b,c); one film is amorphous (b), the other *in situ* polycrystalline (c). The film/substrate interface is indicated by an arrow.

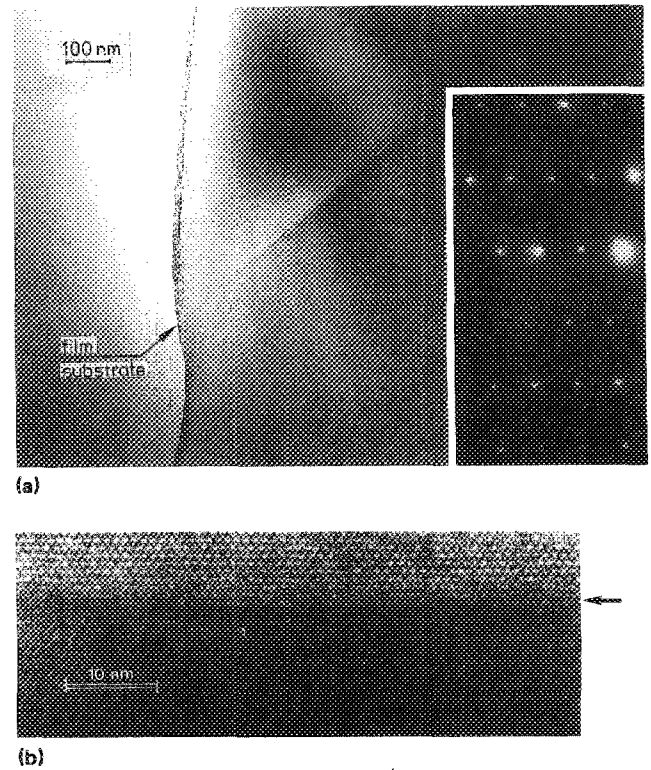

FIG. 5. Transmission electron micrographs (TEM) of a cross section through the film/substrate interface of the rf magnetron-sputtered (110)-oriented epitaxial bismuth-iron garnet film No. 7 with $\Delta a^{\perp} = -1.33 \times 10^{-2}$ nm misfit; (a) bright-field picture with electron diffraction pattern of film No. 7 (insert), the rough edge being an artifact from thinning the specimen by ion milling; (b) lattice image taken along the [111] zone axis of the garnet. The arrows indicate the interface between film (upper part) and substrate. A carbon layer about 10 nm thick was used to avoid charging of the sample.

interface at low and at very high magnification do not reveal any extended or local defects, respectively, as elucidated by Fig. 5. In the lattice image mode of the TEM a perfect alignment of the film with the substrate lattice is observed with no evidence of stacking faults and dislocations even at thicknesses in the 10-μm range. It is emphasized that the sample of Fig. 5 is grown on a (110) substrate under 1% compressive lattice misfit strain, a situation that would not result in epitaxial growth under LPE conditions.

B. Polycrystalline films

Sputtered polycrystalline gadolinium-bismuth-substituted iron-garnet films have been prepared *in situ* at floating substrate potential on ion-bombarded gallium-garnet substrates where epitaxial crystallization is impeded by a bombardment-induced amorphous interface layer of <1 nm thickness.[18] This type of substrate is advantageous over glass substrates with respect to their thermal expansion coefficient, stability, and handling. Films deposited in this way develop a growth-induced uniaxial magnetic anisotropy normal to the film plane, demagnetize in a coarse domain pattern [see Fig. 2(c)], have a rough surface topology with an average feature of 2–5 μm width [see Fig. 2(d)], exceed the magnetic wall coercivity of epitaxial films by at least 2–3 orders of magnitude (see Fig. 3, curve 2), and reveal a columnar morphology in cleaved cross sections normal to the film plane [see Fig. 4(c)]. X-ray and electron diffraction patterns indicate random crystallite orientation, as inferred from Fig. 6 and the insert of Fig. 7(c).

TEM micrographs of cross sections through the film/substrate interface [Fig. 7(a) and 7(b)] elucidate that the film growth in zone I undergoes an initial transient period covering the first about 200 nm of film thickness and corresponding to about a 15-min process time. The 200–400-nm-sized grains in zone I exhibit strong (111) texture [Fig. 7(a)]; some are even epitaxially related with the (111)-oriented garnet substrate. The ion bombardment induced <1-nm-thick amorphous interface layer between substrate and film is clearly discerned [Fig. 7(a)]. This textured coarse-grained zone I is followed by an about 200-nm-thick fine-grained randomly crystallized zone II [Fig. 7(b)] on top of which a columnar-grained zone III has developed with the column axis oriented parallel to the growth direction. The average 70-nm-wide columnar grains have random crystal orientation, as supported by the TEM micrograph of Fig. 7(c) representing a planar section of the film in zone III and

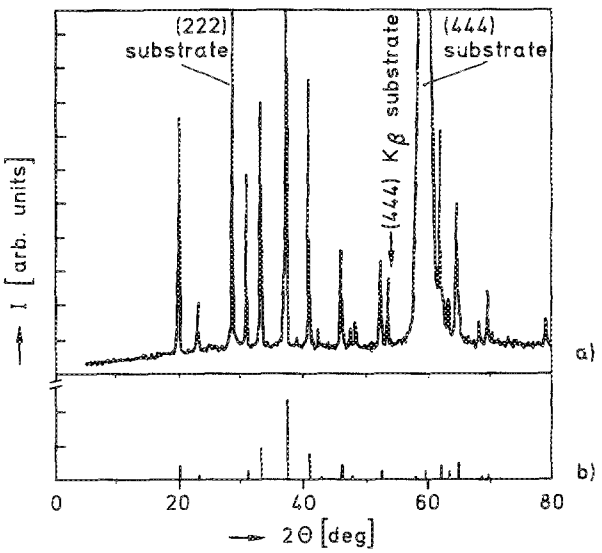

FIG. 6. X-ray diffraction spectra of film No. 6(a) and a powder sample of $Gd_3Fe_5O_{12}$ (b) for comparison; Co$K\alpha$ radiation was used.

by the electron diffraction pattern [insert of Fig. 7(c)]. Their grain boundaries are free of a second phase, as discerned from the lattice image in Fig. 7(d) where four columnar grains are in intimate contact. The macroscopic hillocks observed in the outer film surface [see Fig. 2(d)] are composed of many columns.

Of course, such a granular morphology is not conducive for achieving high readout performance and storage density, in particular because the depth of this irregular nucleation zone I and II exceeds the range of optimal thicknesses of the iron-garnet film, as discussed in Sec. VI.

However, our preliminary experiments show that the film morphology can be much improved by temporarily increasing the dose and energy of the impinging Ar^+ ions from the adjacent plasma sheath during the initial nucleation period. As an example, we have found that a very pronounced (111) texture results in the *whole* film if during the first 15 nm of deposited matter the rf substrate potential is raised to 35 V_{rms} and then reverted to floating electrical potential (~ 3 V_{rms}). Concomitantly, the average energy of the Ar^+ ions is initially increased to about 80 eV and then reduced to about 20 eV at floating potential. Prior to film deposition the substrate had been coated with a 5-nm-thick noncrystalline layer with similar composition as the magnetic film in order to reduce the interfacial energy and to preclude epitaxial growth of the magnetic film. The absence of a coarse nucleation zone, as in Figs. 7(a) and 7(b) is elucidated by the cross-section TEM micrograph in Fig. 8. Furthermore, a strong crystallographic (111) texture is identified from the double-crystal x-ray rocking curve in Fig. 9 that also includes the (888) reflection of the single-crystal GGCMZ substrate beneath the 5-nm-thick amorphous separation layer. To ensure that the lattice of the film and the substrate are not epitaxially aligned and, insofar as possible, simulate the configuration of a garnet film on an arbitrary amorphous substrate, we have compared the apparent "misfit" $\Delta a^{\perp} = -3.76\times10^{-3}$ nm of this film No. 9 with that of the sputter epitaxial film No. 8 with very similar composition, $\Delta a^{\perp} = -8.65\times10^{-3}$ nm. $\Delta a^{\perp}$ can be transformed to the difference Δa_o between the lattice constant of the substrate and the free film by the relation

$$\Delta a_o = \Delta a^{\perp}(1-\mu_{111})/(1+\mu_{111}), \tag{1}$$

where $\mu_{111}=0.3$ is the Poisson ratio. It turns out that $\Delta a_o = -4.66\times10^{-3}$ nm of film No. 8 is still somewhat more negative than $\Delta a^{\perp}$ of film No. 9, and we conclude that the polycrystalline film No. 9 has developed its (111) texture during the initial nucleation period through low-energy ion bombardment independent of the substrate lattice. At later stages of film growth, however, enhanced Ar^+ ion bombardment is unnecessary for maintaining the texture and even undesirable because bismuth would be preferentially backsputtered and the formation of a uniaxial magnetic anisotropy would be suppressed.[16]

These (111) textured iron-garnet films have a fairly smooth surface; in contrast, the hillocks in conventionally sputtered iron-garnet films [Fig. 2(d)] are a direct consequence of the coarse-grained nucleation zone at the substrate interface.

V. OPTICAL AND MAGNETO-OPTICAL PROPERTIES

The optical and magneto-optical properties of rare-earth iron garnets have been reviewed together with the magnetic properties in Ref. 19 and will not be treated here in depth. They are essentially determined by electronic transitions of the Fe^{3+} ions occupying tetrahedrally and octahedrally coordinated lattice sites with O^{2-} ions.[20] A unique substituent on dodecahedral lattice sites, which are typically occupied by rare-earth ions, are the bismuth Bi^{3+} ions that enhance the optical and magneto-optical properties of the Fe^{3+} ions via orbital mixing with the O^{2-} ions and, thereby, increase their spin-orbit coupling and super-exchange interaction.[21] The optical effects are phenomenologically described by the complex dielectric tensor ϵ[20]

$$\epsilon = \begin{pmatrix} \epsilon_{11} & -i\epsilon_{12} & 0 \\ i\epsilon_{12} & \epsilon_{11} & 0 \\ 0 & 0 & \epsilon_{11} \end{pmatrix}, \tag{2}$$

whose complex components ϵ_{12} are related to the observable parameters Faraday rotation Θ_F and ellipticity ϵ_F, Kerr rotation Θ_K and ellipticity ϵ_K, absorption coefficient $\alpha = 4\pi k/\lambda$, and refractive index n, as given in Ref. 20. A detailed account of the optical measurement techniques applied here is presented in Refs. 9 and 10. The component spectra of the dielectric tensor are calculated from these data and presented as unsmoothed curves in the following figures. The real (ϵ'_{11}) and imaginary (ϵ''_{11}) part of the diagonal component ϵ_{11} vs photon energy is given in Fig. 10(a) with increasing bismuth substitution in LPE-grown YIG films containing up to 0.08 Pb [a/gf] and 0.03 Pt [a/gf] as impurities. The photon energy dependence of the real (ϵ'_{12}) and imaginary (ϵ''_{12}) part of the off-diagonal component ϵ_{12} that represents the magneto-optical properties is depicted in Figs. 10(b) and 10(c) with increasing bismuth substitution.

For identification of the major magneto-optically active

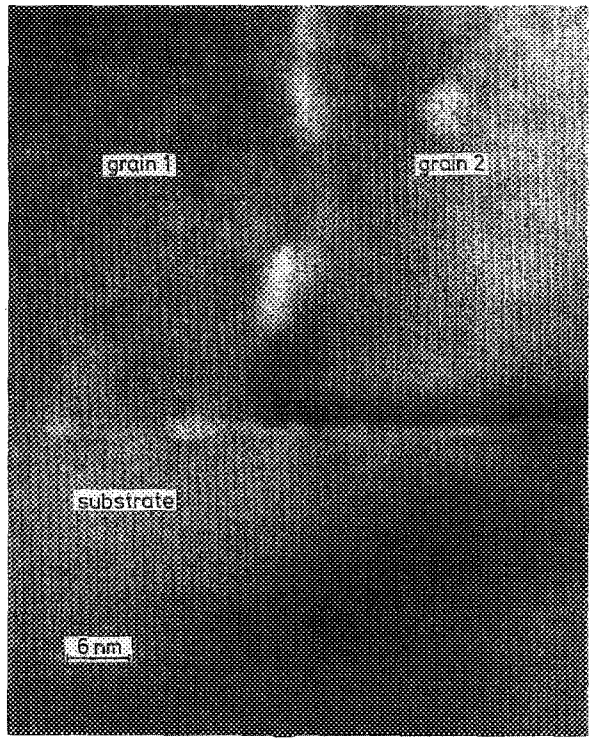

(a)

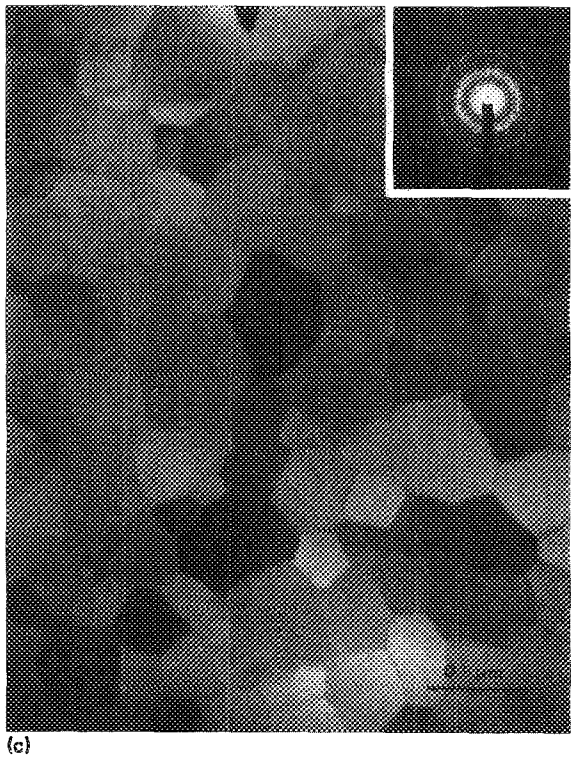

(c)

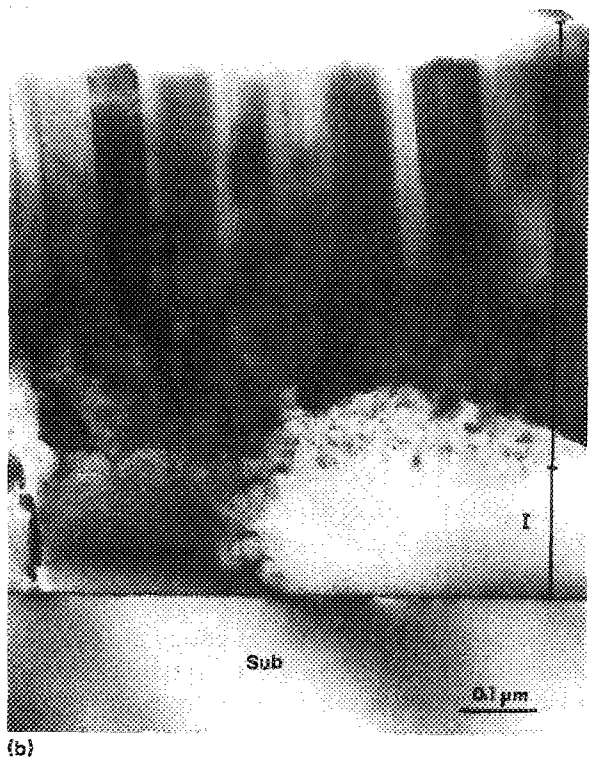

(b)

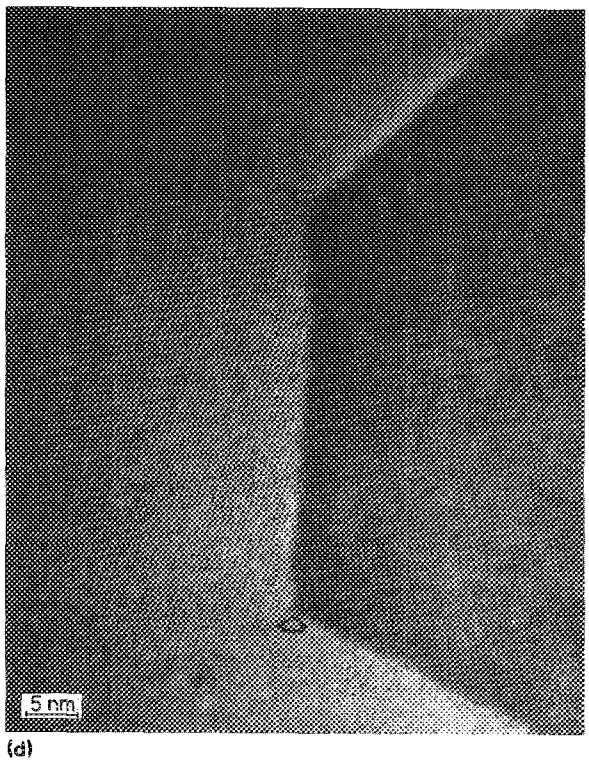

(d)

FIG. 7. TEM micrographs of the polycrystalline rf magnetron sputtered bismuth-iron garnet film No. 6. The cross section through the interface film/substrate at high resolution (a) and at lower resolution (b) reveals the grain structure in the nucleation zone and the < 1-nm-thick amorphous interface layer between substrate and film. The planar section parallel to the film plane through the columnar region at lower (c) and high resolution (d) uncovers the microstructure that has formed after the nucleation period. The electron diffraction pattern made of the columnar region along the film normal [insert in (c)] confirms the random polycrystalline morphology of the columnar part of the film. The lattice images of respective grain boundaries in (a) and (d) elucidate the phase purity of these films.

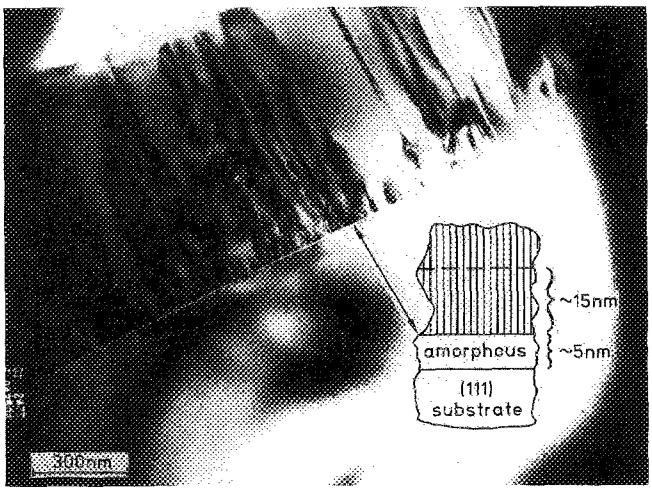

FIG. 8. TEM micrograph of a cross section through the film/substrate interface of sample No. 9. The insert is a magnified view (schematically drawn). No coarse-grained nucleation zone is present, contrary to Fig. 7(b), due to initial low-energy ion bombardment.

transitions we have analyzed the ϵ_{ij} spectra in terms of paramagnetic and diamagnetic line shapes. These can be expressed by the relations[20–22]

$$\epsilon_{xy}^{\text{dia}} = \sum_i K_{1i} \frac{(\omega_{0i}-\omega)^2 - \Gamma_{0i}^2 + 2i\Gamma_{0i}(\omega_{0i}-\omega)}{\omega_{0i}\left[(\omega_{0i}-\omega)^2 + \Gamma_{0i}^2\right]^2},$$

$$\epsilon_{xy}^{\text{para}} = \sum_i K_{2i} \frac{\omega(\omega_{0i}^2 - \omega^2 - \Gamma_{0i}^2) + i\Gamma_{0i}(\omega_{0i}^2 + \omega^2 + \Gamma_{0i}^2)}{\omega_{0i}\left[(\omega^2 - \omega_{0i}^2 - \Gamma_{0i}^2)^2 + 4\omega^2\Gamma_{0i}^2\right]}. \quad (3)$$

Thus, the spectra can be parametrized in terms of the character (dia- or para-) and the frequency ω_{0i} of the involved transitions, the linewidth Γ_{0i}, and the quantum-mechanically determined quantities K_{1i} and K_{2i}. The latter are functions of the number of oscillators with eigenfrequency ω_{0i}, their oscillator strength, and the Zeeman splitting of the involved electronic energy levels by spin-orbit coupling. A detailed account of this analysis will be presented elsewhere.[23]

Taking as an example the spectrum of film No. 1 the components ϵ_{12}' and ϵ_{12}'' can be consistently fitted with a set of values for the three parameters K_{2i}, ω_{0i}, and Γ_{0i} for each of the involved transitions [see Fig. 11(b) and 11(c)] using the values listed in Table IV. When plotting the oscillator amplitude K_{2i} of these transitions versus the bismuth content x[a/gf] in Fig. 12 it turns out that only three transitions are affected. These are located near $\hbar\omega_{0i} = 2.70$ eV (460 nm), 3.40 eV (365 nm), and 4.45 eV (280 nm). They essentially determine the magneto-optical properties of bismuth-substituted iron garnets in the visible and ultraviolet spectrum. On the other hand, the ϵ_{11}'' spectrum has been fitted by Gaussian line shapes of various transitions including those representing the ϵ_{12} spectra [Fig. 11(a)]. The relation used is given by

$$\epsilon_{xx}'' = \sum_i K_i \exp\left[(E - E_{0i})^2/\Gamma_{0i}^2\right], \quad (4)$$

with the parameters of the transitions compiled in Table V.

So far, the assignment of these transitions in terms of basic models has not been fully satisfactory since the choice of line shapes and parameter values is not quite unique because the spectra, at least for smaller x values, are fairly complex.[23]

Polycrystalline iron-garnet films sputtered on glass substrates exhibit similar intrinsic properties as epitaxial films with identical composition. Figure 13 shows the Faraday rotation spectrum of the films No. 1a and 1b.

For optical recording applications in the red and infrared, bismuth-iron garnets exhibit insufficient absorption. The absorption in the red and near-infrared spectrum can be much enhanced by making use of the tetrahedrally coordinated Co^{2+} and Co^{3+} crystal-field transitions in the garnet host where the cobalt ions substitute for Fe^{3+} ions. Strong absorption bands of Co^{2+} ions at 650 (1.91 eV) and 1500 nm (0.83 eV) and of Co^{3+} at 700 (1.77 eV) and 1320 nm (0.94 eV) superimpose on the GIG spectrum,[22,24] as demonstrated for Co^{3+} ions in Fig. 14.

A remarkable feature of sputtering is that, e.g., much more Co^{3+} ions can be forced to enter the garnet lattice than can be reached by LPE. This is because sputtering is operated sufficiently far from thermodynamic equilibrium. Since stronger optical and magneto-optical effects are expected from tetrahedrally coordinated cobalt crystal-field transitons we have analyzed the temperature dependence of the saturation magnetization of these materials in terms of molecular-field theory. It turns out that the distribution of Co^{3+} ions between octahedral and tetrahedral lattice sites is 5.7:1 in film No. 3 and 2.5:1 in film No. 4 when treating the excess Gd^{3+} as occupying octahedral sites as diamagnetic dilution. Thus, occupation of tetrahedral lattice sites by Co^{3+} is favored if film growth is performed at floating substrate potential rather than with substrate bias. Under these

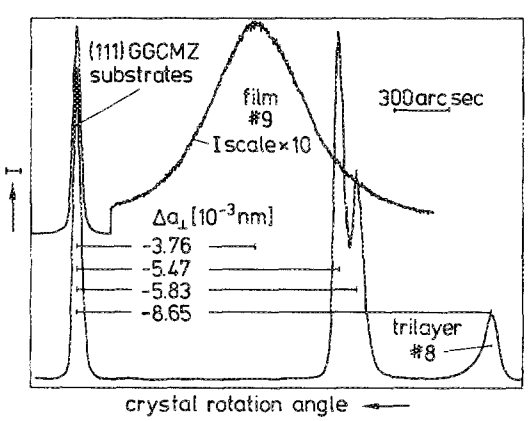

FIG. 9. Double-crystal x-ray rocking curves of film No. 9 (upper trace, scale factor 10) and of an epitaxial trilayer garnet film (lower trace) using (888) Cu$K\alpha_1$ radiation. The trilayer is grown by rf magnetron sputtering at 800 K substrate temperature in 0.6-Pa oxygen-doped argon plasma. The three x-ray diffraction peaks (lower trace, from the right) refer to 0, 0.5, and 1.0 vol % oxygen in the argon plasma, respectively. The sublayer prepared in pure argon plasma (lower trace, right peak) corresponds to film No. 8 (see Table III). The quantity $\Delta a^{\perp} = a_s - a_f^{\perp}$ denotes the difference between the lattice constant of the substrate (a_s) and the perpendicular lattice constant ($a_f^{\perp}$) of the films.

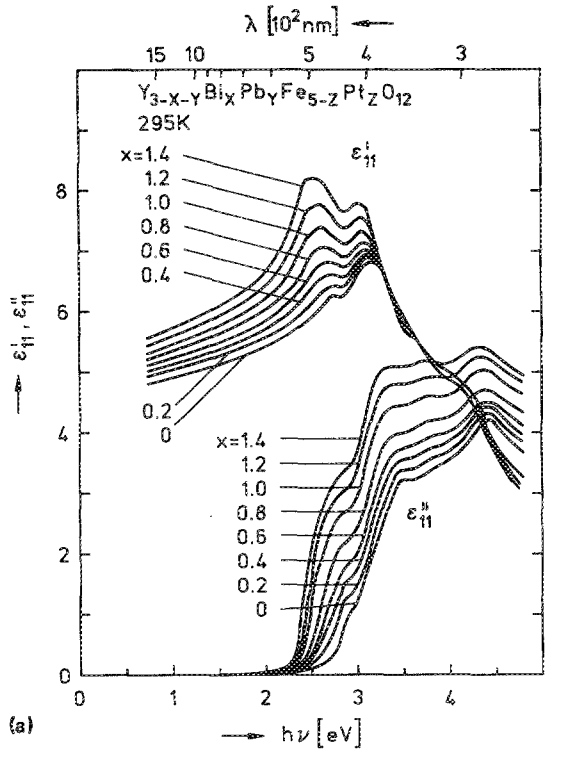

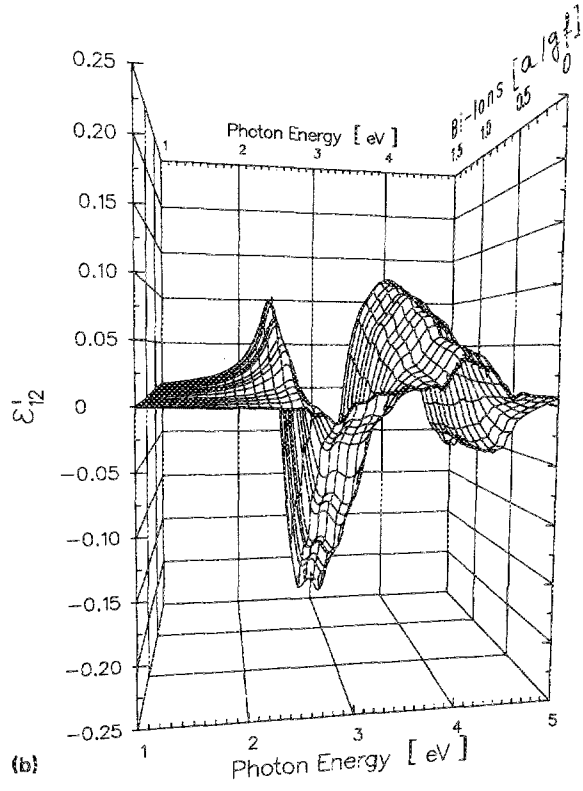

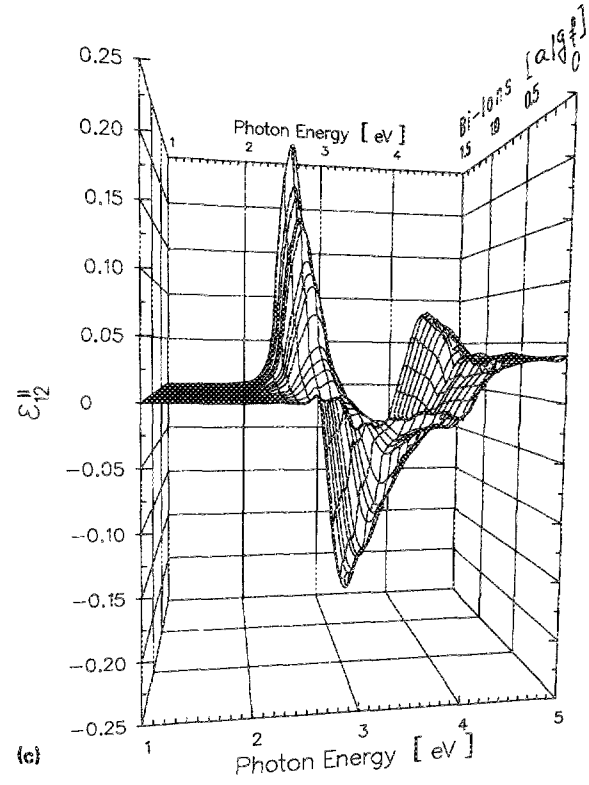

FIG. 10. Calculated unsmoothed spectra of the elements ϵ'_{11} and ϵ''_{11} (a), ϵ'_{12} (b), and ϵ''_{12} (c) of the dielectric tensor ϵ for $Y_{3-x}Bi_xFe_5O_{12}$ films prepared by liquid-phase epitaxy, using the spectroscopic data reported in Refs. 9 and 10. The thick curve in Figs. 10(b) and 10(c) (foreground) refers to $x=0$; increments $\Delta x=0.1$ [a/gf] between consecutive curves; $y\leqslant 0.06$[a/gf] and $z\leqslant 0.03$[a/gf]. Spectra measured at 295 K.

assumptions the agreement between the molecular-field fits and the measured magnetization is satisfactory, as shown in Fig. 15(a) and 15(b). The magneto-optical activity of cobalt ions in iron garnets in the near infrared is presented in Fig. 16. The strong transition bands at about 1350 nm (0.92 eV, tetrahedral Co^{3+}) and 1500 nm (0.83 eV, tetrahedral Co^{2+}), exhibiting paramagnetic and diamagnetic line shapes, respectively, correspond to those in the optical absorption spectra, shown in Fig. 14 for Co^{3+}. The strong magneto-optical transition around 650 nm (1.91 eV, tetrahedral Co^{2+})[24] and the broadband around 700 nm (1.77 eV, octrahedral Co^{3+})[22] are not resolved, however, since they superimpose on the tail of the even stronger Fe^{3+} transitions in the blue and ultraviolet.

The barium hexaferrites exhibit a shift of the fundamental absorption band edge to the infrared by several tenths of

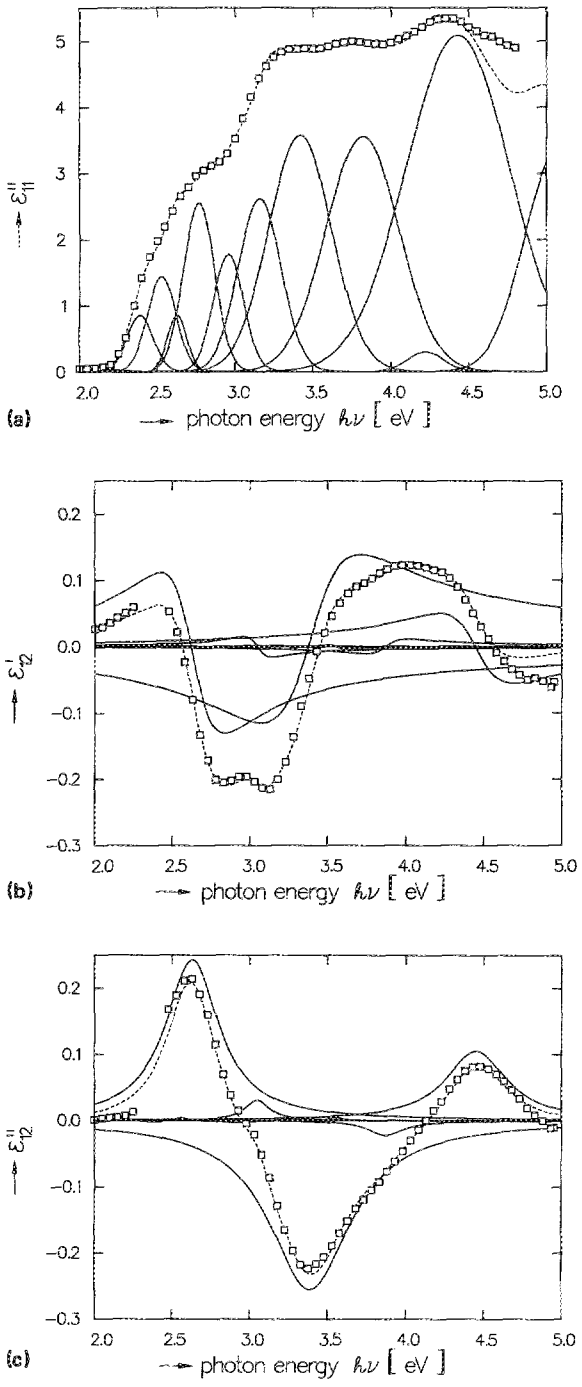

FIG. 11. Comparison between the measured ϵ''_{11} (a), ϵ'_{12} (b), and ϵ''_{12} (c) spectra of film No. 1 and calculated spectra using Gaussian (a) and paramagnetic (b,c) line shapes for the involved optical transitions. The frequency dependence of the paramagnetic transitions is given by Eq. (3) using the parameters ω_{0i}, Γ_{0i} and K_{2i} for each transition as listed in Table IV. The transition parameters fo the Gaussian lines are listed in Table V. Open squares denote the measured values of these spectra and the dashed curves represent the calculated spectra (see Ref. 23). Experimental data at 295 K.

an electron volt, as compared to iron garnets. Pronounced effects on the optical properties of the pure $BaFe_{12}O_{19}$ can be achieved by manganese substitution of Fe^{3+} (see Fig. 17). On the other hand, the magneto-optical activity of this class of materials in the 550–450 nm (2.25–2.76 eV) spectral range is fairly low (see Fig. 18) and enhancement by bismuth substitution has failed so far.

TABLE IV. Parameters of the magneto-optically active paramagnetic transitions of film No. 1 [Figs. 11(b), 11(c), and 12] when using the frequency dependence as in Eq. (3).

E_{0i} (eV)	Γ_{0i} (eV)	K_{2i}
2.38	0.055	−0.0006
2.56	0.038	0.0008
2.63	0.210	0.2680
2.91	0.095	−0.0018
3.05	0.095	0.0180
3.24	0.035	0.00055
3.39	0.320	−0.5530
3.55	0.042	0.00165
3.87	0.140	−0.0240
4.45	0.240	0.2250

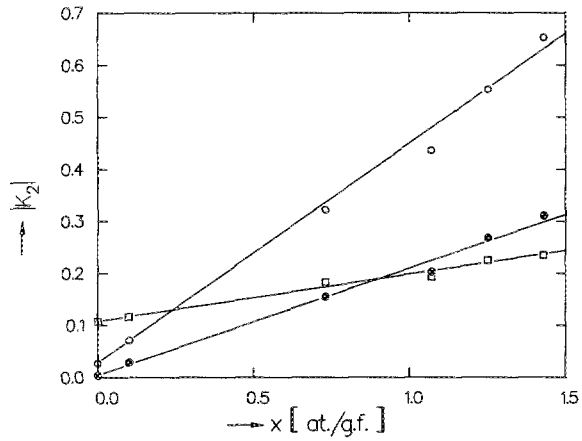

FIG. 12. Oscillator amplitude $|K_{2i}|$ of those paramagnetic transitions sensitive to the bismuth concentration x in the LPE-grown $Y_{3-x}Bi_xFe_5O_{12}$ films whose dielectric tensor components are depicted in the Figs. 10 and 11; full circles: transition at $h\nu_i \approx 2.63$ eV; open circles: transition at $h\nu_i \approx 3.40$ eV, and open squares: transition at $h\nu_i \approx 4.45$ eV (see Table IV) (see Ref. 23). Experimental data at 295 K.

TABLE V. Parameters of the optical [Fig. 11(a)] transitions identified in film No. 1 [Fig. 11(a)] when using Gaussian line shapes as in Eq. (4).

E_{0i} (eV)	Γ_{0i} (eV)	K_i
1.78	0.191	0.019
2.08	0.212	0.040
2.39	0.099	0.860
2.53	0.108	1.440
2.63	0.072	0.860
2.77	0.117	2.560
2.96	0.114	1.780
3.16	0.162	2.620
3.42	0.237	3.580
3.82	0.275	3.560
4.22	0.133	0.300
4.43	0.391	5.090
5.07	0.250	3.330

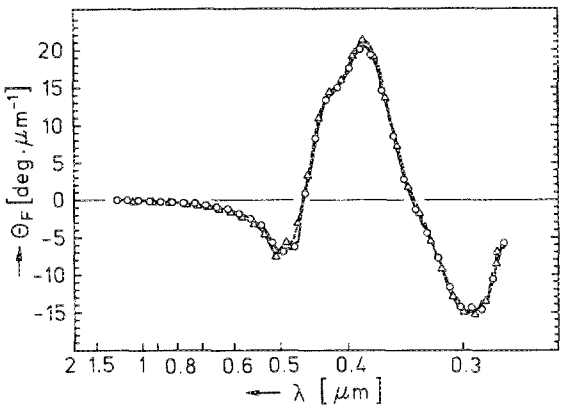

FIG. 13. Faraday rotation spectrum of the LPE film No. 1a and the sputtered polycrystalline film No. 1b on glass; data at 295 K.

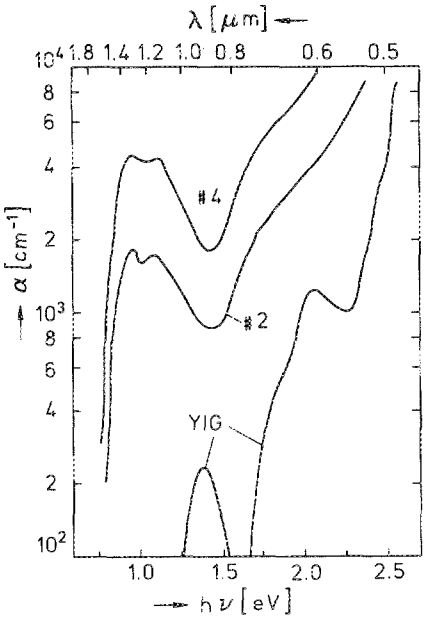

FIG. 14. Increase of optical absorption by Co^{3+} substitution into iron-garnet films, as exemplified by the spectra of the sputtered GdFeCo-garnet films No. 2 and 4 and pure YIG. Data at 295 K.

VI. COMPARISON BETWEEN THE MAGNETO-OPTICAL PERFORMANCE OF AMORPHOUS RARE-EARTH TRANSITION-METAL FILMS, Co/Pt MULTILAYERS, AND IRON-GARNET FILMS

At an 800-nm wavelength, the CNR in today's RETM disks is mainly limited by noise arising from noncylindrical domain walls, from ripple in the magnetization direction, and from surface roughness. Improvements in the storage capacity within the present recording concept can be achieved, e.g., by reducing the laser wavelength and by multilevel recording where several storage layers are stacked upon each other. The magneto-optical performance of new memory media needs not to be better than that of RETM films at 800 nm if the noise sources just mentioned are not reduced at the same time, because otherwise the noise level would be raised, simultaneously. However, these noise sources are essentially process dependent and not yet mastered in rf sputtering of polycrystalline iron-garnet films. Pioneering work has been performed by Gomi *et al.*,[5] Itoh *et al.*,[6] and Shono *et al.*[6] but much has still to be done to understand and improve the process.

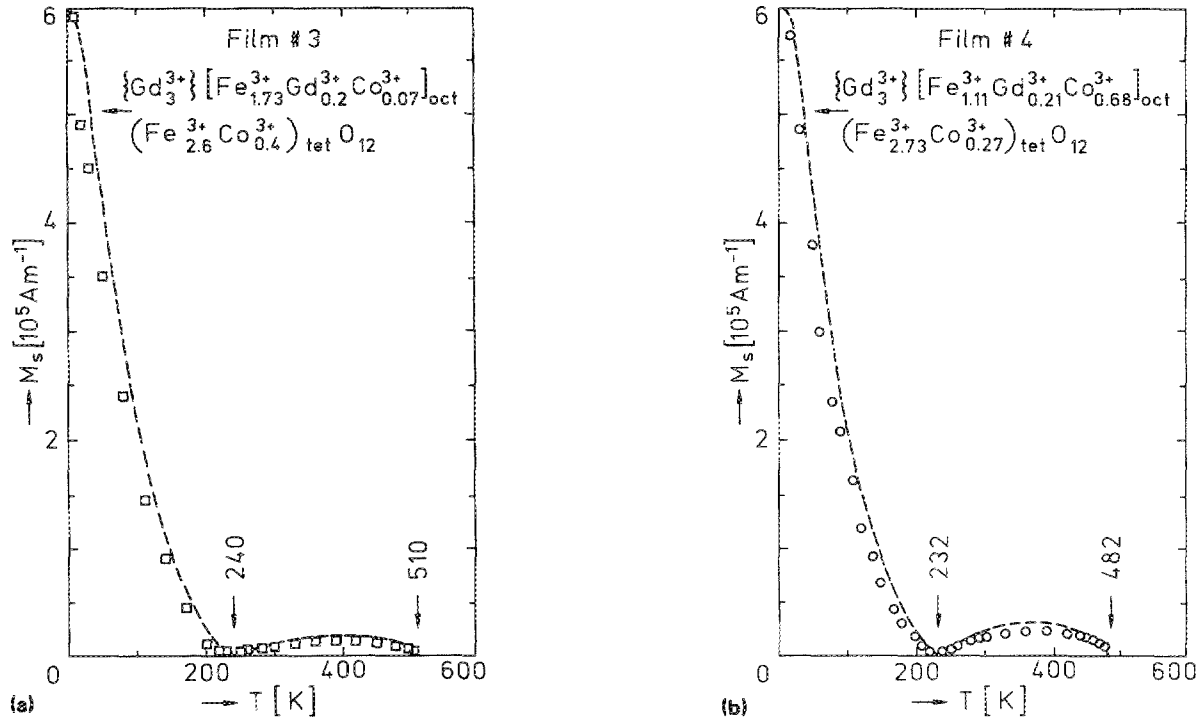

FIG. 15. Temperature dependence of the saturation magnetization M_s of the Co^{3+}-substituted iron-garnet films Nos. 3 (a) and 4 (b). Open circles and squares, respectively, represent measured data and the broken curves represent theoretical fits by molecular-field theory using the lattice site occupation given by the chemical formulas in the figure.

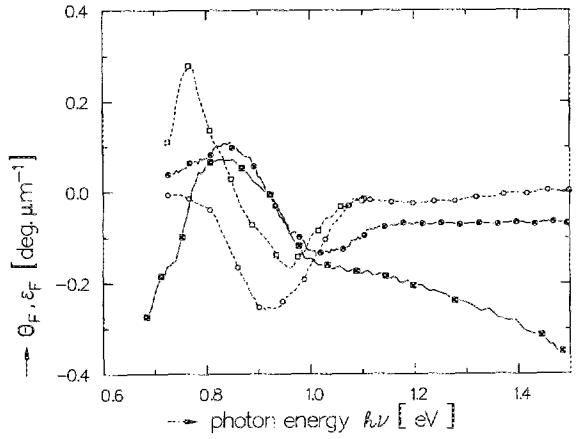

FIG. 16. Measured Faraday rotation Θ_F (full symbols) and ellipticity ϵ_F (open symbols) of the Co^{3+}-substituted film No. 4 (scaled down to $\frac{1}{10}$ of values) and the Co^{2+}-substituted film No. 5. Circles represent film No. 4 and squares film No. 5. Data at 295 K.

In this section we restrict ourselves to the *intrinsic* magneto-optical performance and compare RETM films and Co/Pt multilayers with iron-garnet films in the wavelength regime from 820 to 420 nm. In Fig. 19(a) the absorption spectra of a TbFe and a highly bismuth-substituted YIG film are plotted against the wavelength, supplemented in Fig. 19(b) by the Faraday rotation spectra, and in Fig. 19(c) by the magneto-optical figure of merit in transmission. Using the optical data presented in this article we calculate the magneto-optical reflectance of the magnetic film which rests on a 100% mirror composed of 25 dielectric layers with periodic refractive index steps. The computer program developed by Kivits[25] makes use of a matrix calculus for stratified media. It is based on the concept that the phase and amplitude of the right and left circularly polarized component of the impinging light beam are individually affected by the birefringent and dichroic properties of the magnetic film and that these modes interact coherently with those of the reflected beam.

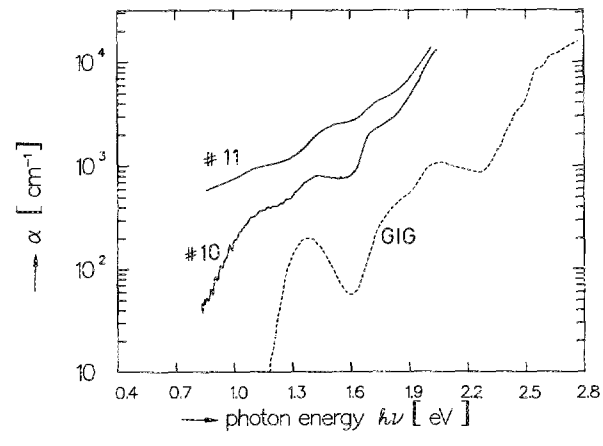

FIG. 17. Optical absorption spectra of the barium hexaferrite samples No. 10 and 11 in comparison to $Gd_3Fe_5O_{12}$. Sample No. 11 contains 0.17 manganese [a/gf] on Fe^{3+} sites. Data at 295 K.

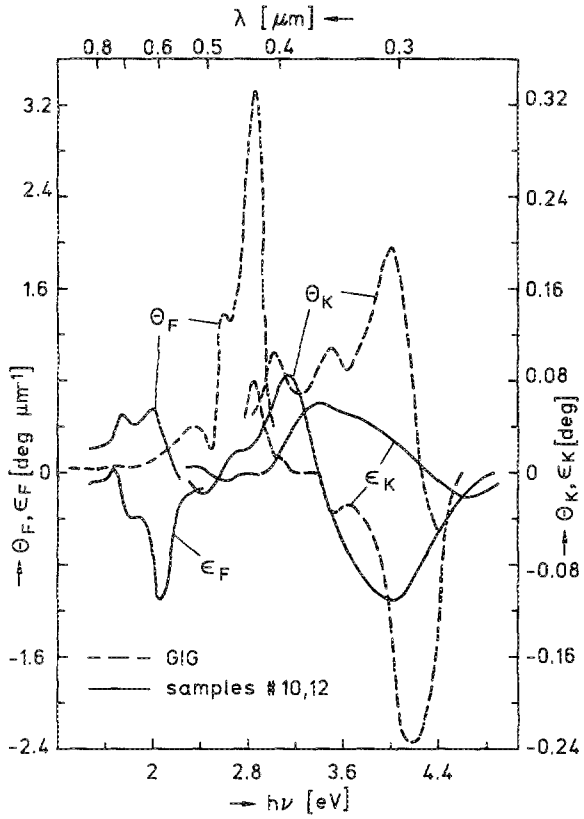

FIG. 18. Magneto-optical Faraday (Θ_F, ϵ_F) and Kerr (Θ_K, ϵ_K) spectra of $Gd_3Fe_5O_{12}$ and $BaFe_{12}O_{19}$. Data at 295 K.

The following observations are deduced from this analysis: At a certain thickness d of the magnetic film the magneto-optical azimuth rotation in reflection, Θ'_K undergoes significant interference enhancement, concomitant with increased absorbed light power ($1-R-T$) at the expense of total reflected light power R. There is a trade-off between Θ'_K and R for intermediate values of d, as shown in Fig. 20 for the iron-garnet film No. 1a at the wavelength $\lambda = 488$ nm. In this case the first interference maximum of Θ'_K appears at $d = 103$ nm, the second at $d = 197$ nm accomodating approximately one half and one effective wavelength of light within the magnetic layer, respectively. The quantities Θ'_K and ϵ'_K arise from a superposition of Faraday and Kerr effects, rather than the intrinsic Kerr rotation (Θ_K) and ellipticity (ϵ_K) alone. The parameter $[\Theta'^2_K + \epsilon'^2_K]R$ represents the magneto-optical figure of merit of recording media for readout in reflection.

In Table VI(a) we summarize the calculated magneto-optical performance data of iron-garnet films on a 100% interference mirror for four different wavelengths. For comparison, the magneto-optical performance data of a conventional GdTbFe trilayer have also been calculated[26] and are presented in part (b) of Table VI. For obtaining a CNR > 60 dB required in recording systems these values ($|\Theta'_K| \approx 1°$, $R \approx 20\%$, $d < 100$ nm) are considered as close to the tolerated limit for recording and are taken here as reference to evaluate the performance of new media.

It becomes evident that the magneto-optical perfor-

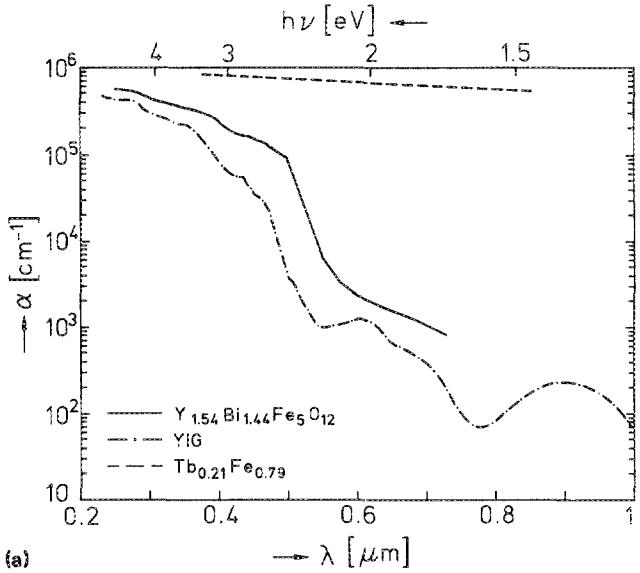

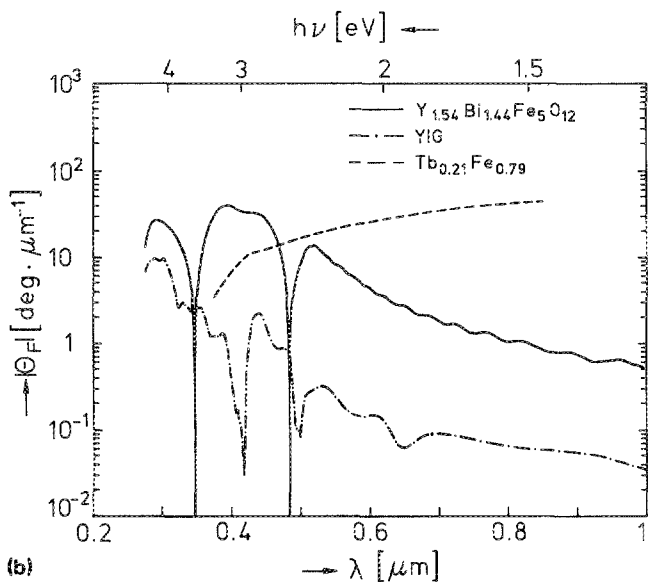

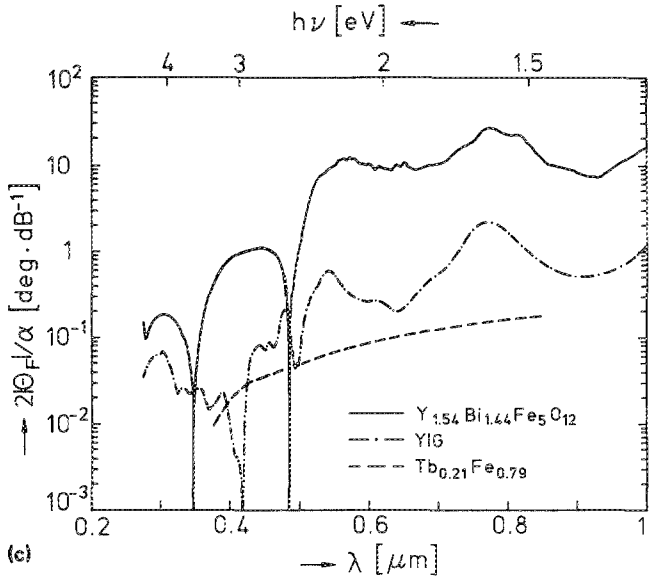

FIG. 19. Comparison between the absorption (a), Faraday rotation (b), and figure of merit (c) spectra of LPE-grown $(Y,Bi)_3Fe_5O_{12}$ and $Y_3Fe_5O_{12}$ films and an evaporated TbFe film to be used in Table VI. Data at 295 K.

mance of RETM media is limited by the fact that these materials cannot be operated at interference due to high optical absorption. It is shown for TbFe in part (a) of Table VI when taking optical data from Ref. 27, that interference effects are only significant at thicknesses < 10 nm. Furthermore, the magneto-optical Kerr effects of GdTbFe films are weaker at shorter wavelengths, so that their application at shorter wavelengths for achieving higher storage density can be ruled out.

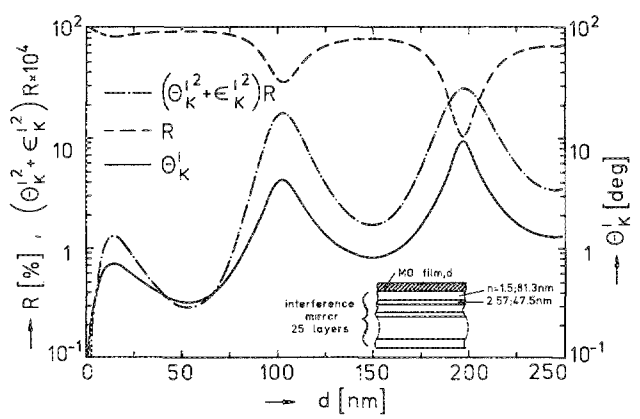

FIG. 20. Calculated magneto-optical figure of merit in reflection $[\Theta_K'^2 + \epsilon_K'^2]R$, total reflectance R, and azimuth rotation in reflection Θ_K' vs thickness d of the magnetic film No. 1a on top of a 100% interference mirror for $\lambda = 488$ nm. The layer sequence is given in the insert.

In contrast, bismuth-substituted iron-garnet films are increasingly attractive for optical recording when reducing the wavelength towards the strong magneto-optically active transitions in the blue ($\lambda \approx 460$ nm) and ultraviolet ($\lambda \approx 365$; 280 nm), as can be seen in part (a) of Table VI. Setting $R \approx 20\%$ and $d < 100$ nm some enhancement of the optical absorption is needed in the red spectrum, e.g., by cobalt substitution into the iron garnet (here indicated by No. 1a + Co), while in the green and blue spectrum the values of Θ_K' and $[\Theta_K'^2 + \epsilon_K'^2]R$ are much superior to those exhibited by conventional GdTbFe media at an 800-nm wavelength.

An additional advantage of iron-garnet films is the possibility of conceiving a multilayer recording medium by making use of the favorable magnitude of optical absorption.

This comparative study is supplemented by mentioning Co/Pt multilayers, a very recent material whose magneto-

TABLE VI. (a) Calculated magneto-optical figure of merit in reflection $[\Theta_K'^2 + \epsilon_K'^2]\,R$, total reflectance R, and azimuth rotation in reflection Θ_K' of an iron-garnet film with thickness d on top of a 100% interference mirror at several wavelengths λ; d is chosen at the first two interference extrema seen in Fig. 20; n denotes the refractive index, k the extinction coefficient, and $(1 - R - T)$ the light power absorbed in the magnetic film. The materials $x = 1.0$ and 1.5 stand for $Y_2Bi_1Fe_5O_{12}$ and $Y_{1.5}Bi_{1.5}Fe_5O_{12}$, respectively; material No. 1a + Co denotes film No. 1a with Co-enhanced optical absorption. (b) Calculated magneto-optical reflectance of a conventional trilayer film composed of a glass substrate, an AlN antireflection coating, a magneto-optical GdTbFe film with thickness d and an Al mirror. (c) Calculated magneto-optical reflectance of a Co/Pt multilayer with total thickness d on a glass substrate and coated with and AlN antireflection layer.

λ (nm)	Material	Interference maximum	d (nm)	n	k	Θ_K (deg)	ϵ_K (deg)	Θ_K' (deg)	R (%)	$(\Theta_K'^2 + \epsilon_K'^2) \times 10^4 R$	$(1 - R - T)$ (%)
					(a) Magneto-optical film on 100% multilayer interference mirror						
420	$x = 1.0$	first	82.2	2.60	0.257			15.19	1.24	8.74	98.8
420	$x = 1.5$	first	74.7	2.85	0.334			17.40	0.57	5.25	99.4
488	No. 1a	first	103.0	2.57	0.078			4.18	32.00	17.08	67.4
488	No. 1a	second	196.8	2.57	0.078			9.51	10.40	28.70	89.6
633	No. 1a + Co	first	135.0	2.40	0.040			1.68	60.00	5.25	
633	No. 1a + Co	second	260.0	2.40	0.040			3.40	36.00	13.20	
800	No. 1a + Co	second	349.0	2.30	0.024			0.33	54.3	0.18	45.6
800	TbFe[a]	first	4.3	3.54	3.76			45.00	0.03	3.50	99.9
					(b) Trilayer glass AlN/GdTbFe/Al						
820	GdTbFe[b]	too thick	40.0	3.57	3.32	−0.24	−0.08	−0.96	20.10	0.56	75.9
					(c) Multilayer glass AlN/4-Å Co/9-Å Pt/4-Å Co/9 Å Pt/...						
820	Co/Pt[b]	too thick	18.0	3.11	5.07	−0.20	0.05	−0.99	19.20	0.63	67.3
420	Co/Pt[b]	too thick	24.0	1.65	2.94	−0.36	0.10	−1.11	18.60	0.69	68.2

[a] Data from Ref. 27.
[b] Data from Ref. 26.

optical properties do not degrade when reducing the wavelength towards the ultraviolet spectrum.[26] In part (c) of Table VI calculated data on the magneto-optical performance in reflection of a multilayer stack composed of a glass substrate, AlN antireflection coating and a periodically repreated sandwich of 4-Å Co and 9-Å Pt having a total thickness d are presented. As compared to RETM films this material has improved chemical stability and satisfactory readout performance in the blue but slightly higher Curie temperature and a microcrystalline morphology. The optical absorption is too high for exploiting optical interference effects on Θ_K'.

VII. CONCLUSION

From the viewpoint of *intrinsic* magneto-optical performance the bismuth-substituted iron garnets are attractive contenders for reversible optical recording in the blue and near-ultraviolet spectrum. Since interference enhancement can be used the iron garnets are, also, candidates for multilevel recording. Furthermore, their stability and some aspects of magnetron sputtering to prepare this material in thin-film form are superior to RETM media. Like RETM alloys, the iron garnets can be tailored to meet system requirements by chemical substitution; they exhibit an adjustable magnetic compensation temperature to minimize demagnetizing effects, and adjustable Curie temperature to optimize the write-in sensitivity. Under favorable sputtering conditions iron-garnet films develop a perpendicular magnetic anisotropy and crystallize in a textured columnar morphology.

The newly reported Co/Pt multilayer media exhibit improved magneto-optical performance at shorter wavelengths and a much better chemical stability as compared to RETM media, but do not reach the shorter-wavelength performance of bismuth-iron garnets. Furthermore, Co/Pt multilayers cannot be applied to multilayer recording.

Whether iron garnets will become a future generation magneto-optical recording medium essentially relies on the mastering of process-dependent microstructure-related properties, like magnetic wall coercivity and magnetic remanence. Other questions to be answered relate to the feasibility of using glass substrates and making grooves for tracking.

ACKNOWLEDGMENTS

We gratefully acknowledge the supply of substrates from D. Mateika and ceramic sputter targets from F. Welz, the EPMA work by D. Obertop and P. Willich, the x-ray diffraction analysis by B. Strocka, some of the TEM work by B. Koek, the supply of LPE-grown Co^{2+}-substituted iron-garnet films by C.-P. Klages, and sputtering of some of the films by R. Eckart and H. Meyer. We thank D. Mergel, W. Tolksdorf, and W. B. Zeper for fruitful discussions.

[1] Y. Kaneko, Y. Sawada, F. Ohmi, I. Miyamoto, and A. Watada, Jpn. J. Appl. Phys. **26S**, 23 (1987).
[2] Y. Hoshi, M. Naoe, and S. Yamanaka, Proceedings of the International Ion Engineering Congress, Kyoto, 1983, p. 1017.
[3] M. Matsuoka, Y. Hoshi, M. Naoe, and S. Yamanaka, IEEE Trans. Magn. **MAG-18**, 1119 (1982).
[4] K. Shono, H. Kano, N. Koshino, and S. Ogawa, IEEE Trans. Magn. **MAG-23**, 2970 (1987).
[5] M. Gomi, T. Okazaki, and M. Abe, IEEE Trans. Magn. **MAG-23**, 2967 (1987).
[6] A. Itoh, W. R. Eppler, D. Shieh, and M. Kryder, Twelfth International Colloquium Magnetic Film Surfaces, Le Creuzot, 1988, Paper No. W1-05; K. Shono, S. Kuroda, H. Kano, N. Koshino, and S. Ogawa, Materials Research Society Meeting, San Diego, 1989, Paper No. F3-02.

[7]J. W. D. Martens and A. B. Voermans, IEEE Trans. Magn. **MAG-20**, 1007 (1984).
[8]J.-P. Krumme, V. Doormann, B. Strocka, K. Witter, and H. Hemme, J. Appl. Phys. **62**, 3879 (1987).
[9]J.-P. Krumme, V. Doormann, and C.-P. Klages, Appl. Opt. **23**, 1184 (1984).
[10]V. Doormann, J.-P. Krumme, and C.-P. Klages, Appl. Phys. A **34**, 223 (1984).
[11]P. Hansen, K. Witter, and W. Tolksdorf, Phys. Rev. B **27**, 6608 (1983).
[12]H. Dötsch, D. Mateika, P. Röschmann, and W. Tolksdorf, Mater Res. Soc. Bull. **18**, 1209 (1983).
[13]P. Röschmann, M. Lemke, W. Tolksdorf, and F. Welz, Mater Res. Soc. Bull. **19**, 385 (1984).
[14]J.-P. Krumme, V. Doormann, and R. Eckart, IEEE Trans. Magn. **MAG-20**, 983 (1984).
[15]W. Tolksdorf, IEEE Trans. Magn. **MAG-11**, 1074 (1975).
[16]J.-P. Krumme, V. Doormann, H. Lenz, and H. Meyer (unpublished).
[17]J.-P. Krumme, A. F. Otterloo, P. C. Zalm, and J. Petruzzello, J. Appl. Phys. **64**, 3965 (1988).
[18]J.-P. Krumme, V. Doormann, B. Strocka, and P. Willich, J. Appl. Phys. **60**, 2065 (1986).
[19]P. Hansen and J.-P. Krumme, Thin Solid Films **114**, 69 (1984).
[20]F. J. Kahn, P. S. Pershan, and J. P. Remeika, Phys. Rev. **186**, 891 (1969).
[21]S. Wittekoek, T. J. A. Popma, J. M. Robertson, and P. F. Bongers, Phys. Rev. B **12**, 2777 (1975).
[22]A. Abraham, J. Cermak, L. Kalivoda, M. Nevriva, and Z. Simsa, IEEE Trans. Magn. **MAG-24**, 1853 (1988); Z. Simsa, IEEE Trans. Magn. **MAG-23**, 3323 (1987).
[23]V. Doormann, J.-P. Krumme, and H. Lenz (unpublished).
[24]D. L. Wood and J. P. Remeika, J. Chem. Phys. **46**, 3595 (1967).
[25]P. J. Kivits, Philips Research Lab. Eindhoven, The Netherlands (private communication).
[26]W. B. Zeper, F. J. A. M. Greidanus, and P. F. Carcia, Proceedings of the Magnetism and Magnetic Materials Conference, 1989 [IEEE Trans. Magn. (to be published)].
[27]R. Allen and G. A. N. Connell, J. Appl. Phys. **53** 2353 (1982).